frontiers | Frontiers in Earth Science

TYPE Original Research
PUBLISHED 28 August 2023
DOI 10.3389/feart.2023.1176458

OPEN ACCESS

EDITED BY
Andrew R. Thurber,
Oregon State University, United States

REVIEWED BY
Entao Liu,
China University of Geosciences Wuhan, China
Pavlos Megalovasilis,
University of Patras, Greece

*CORRESPONDENCE
Chunhui Tao,
taochunhui@sio.org.cn

RECEIVED 28 February 2023
ACCEPTED 14 August 2023
PUBLISHED 28 August 2023

CITATION
Yang X, Tao C and Liao S (2023), Abundant off-axis hydrothermal activity in the 29–30 ridge segment of the Southwest Indian Ridge: evidence from ferromanganese crusts.
Front. Earth Sci. 11:1176458.
doi: 10.3389/feart.2023.1176458

Abundant off-axis hydrothermal activity in the 29–30 ridge segment of the Southwest Indian Ridge: evidence from ferromanganese crusts

Xianhui Yang[1,2], Chunhui Tao[1,2]* and Shili Liao[1,2]

[1]School of Oceanography, Shanghai Jiao Tong University, Shanghai, China, [2]Key Laboratory of Submarine Geosciences, Second Institute of Oceanography, Ministry of Natural Resources, Hangzhou, Zhejiang, China

In the ultra-slow spreading mid-ocean ridge, seafloor hydrothermal ventings mostly occur in the off-axis region. The plume of hydrothermal venting provides Fe, Mn and other metal materials for the growth of ferromanganese crust in the surrounding seamounts, showing unique geochemical characteristics that are different from that of hydrogenetic crust. Based on five samples of ferromanganese crusts, major, trace and rare earth element analysis was carried out to identify their material sources. Combined with the investigation data of water column and seafloor camera photos by deep towed hydrothermal detection system, the potential of hydrothermal activity in the 29–30 ridge segment of the Southwest Indian ridge was evaluated. The results showed that the ferromanganese crust in the study area had significantly higher Fe/Mn value (average 1.9), relatively higher Si and Al contents, and significantly higher Ca/P value (average 9.3),without significant phosphorylation. ferromanganese crust in the study area have significantly lower Co and Ni contents (about 1600 mg/kg on average), and relatively lower Sr, Ba, Pb, Cu, Zr and Mo contents (between 100-1000 mg/kg on average). The contents of W, Th and Te are also relatively low (average content between 10–50 mg/kg); The total rare earth element content of the crust in the study area is relatively low (about 928 mg/kg on average), and the light rare earth is relatively enriched. The standardized rare earth curve of the shale shows a left-leaning pattern as a whole, showing the enrichment of heavy rare earth relative to the shale. The Co content and rare earth element content of the ferromanganese crusts in this area are significantly lower than those of hydrogenetic crusts. The discrimination diagrams of ternary and bivariate material sources reveal that they have mixed hydrothermal and hydrogenetic origins. The three crust samples of S1, S2, and S5 are located within 2 km of the known hydrothermal fields, indicating a correlation between ferromanganese crust and the location of hydrothermal activity. There is no known hydrothermal field near the S3 and S4 stations. Altered rocks and water column turbidity anomalies were found near S3 station, and large areas of altered rocks and suspected hydrothermal biological remains were also found near S4 station, indicating that hydrothermal activity may exist in both areas. In addition to the two new hydrothermal fields identified in this article, the spatial frequency of hydrothermal activity in the study area reaches 15 sites/100 km, which is significantly higher than other well investigated oceanic ridges. Out of the eight hydrothermal fields in the study area, seven are located in the off axis region,

mainly because the hydrothermal activity in this area is controlled by high angle and large offset normal faults and one-way detachment faults. This also indicates that the off-axis region of the Southwest Indian Ridge has high potential for hydrothermal activity.

KEYWORDS

Southwest Indian Ridge, ultra-slow spreading, off-axis, hydrothermal activity, ferromanganese crust, tectonic-controlled

1 Introduction

Seafloor polymetallic sulfide deposits are layered or stratabound sulfide deposits formed at or near the seafloor hydrothermal vents (Hannington et al., 2005). The deposits are formed at the hydrothermal vent by high-temperature, metal-rich and sulfur-rich fluid mixed with cold seawater and precipitated sulfide minerals (Hannington et al., 2011). Since the first discovery of seafloor hydrothermal vents, it has been known that seafloor hydrothermal ventings may occur in all mid-ocean ridges and ocean basins (Beaulieu et al., 2015). The discovery of seafloor hydrothermal fields is mainly concentrated in the slow-fast spreading ridges, such as the East Pacific Rise, the Central Indian Ridge, the Mid-Atlantic Ridge, etc. (Baker et al., 2016), but relatively few hydrothermal fields were found in ultra-slow spreading ridges, such as the Southwest Indian Ridge. In the slow-ultra slow-spreading ridge, "too many" high-temperature hydrothermal venting fields have been found, which may be because tectonic activity plays a greater role in the hydrothermal circulation than the magma supply (Beaulieu et al., 2015; German et al., 2016). It has been found that half of the high-temperature hydrothermal venting of the North Mid-Atlantic Ridge is controlled by tectonic activities (Escartín et al., 2008; Fouquet et al., 2010). In the slow-ultra slow-spreading ridge, the tectonically controlled seafloor hydrothermal activity often deviates from the ridge axis by 0–10 km. They have stable hydrothermal circulation fluid channels and stable heat sources and can maintain long-term hydrothermal activity for tens to hundreds of thousands of years (Tivey et al., 2003; Tao et al., 2020; Wu et al., 2021). This type of hydrothermal system will play an important role in both the formation of large-scale polymetallic sulfide deposits and the stable and long-term input of a large number of trace elements into the ocean.

The seafloor hydrothermal activity survey was initially started by the on-site observation of manned or unmanned submersibles on the seabed (Baker et al., 2016). The scope of the survey is very small, and there are few hydrothermal activity areas found. The plume of seafloor hydrothermal venting has unique physical, chemical and optical characteristics that are different from the surrounding seawater: such as temperature, salinity, turbidity, oxidation-reduction potential, methane and other abnormal parameters (Baker, 2017). Near-bottom detection of hydrothermal plumes is the most widely used technical method to investigate seafloor hydrothermal activities at present (German et al., 2016). In the database of seafloor hydrothermal fields published by Inter Ridge, about 80% of them were discovered by hydrothermal plume detection (Beaulieu and Szafrański, 2020). However, all hydrothermal activities will eventually stop. For inactive seafloor hydrothermal fields, there is no signal of hydrothermal plume, which is difficult to find. In the database, only 54 are identified as inactive. These inactive hydrothermal areas have undergone a complete hydrothermal circulation, and the accumulated polymetallic sulfide deposits are larger in scale and can avoid the risk of damaging the ecosystem near the active hydrothermal vents, which is conducive to marine mining and has attracted more attention (Jamieson and Gartman, 2020).

Ferromanganese crusts are commonly found on seamounts or ridges in ocean basins, which are precipitated by hydroxyl iron oxide and manganese oxide in seawater, and are rich in Fe, Mn, Co, Cu, Ni, rare earth elements (REE) and other metal elements (Hein and Koschinsky, 2014). In the vicinity of ocean ridges or hot spots, seafloor hydrothermal ventings provide rich Fe and Mn for the formation of ferromanganese crusts. Due to the high growth rate of crusts, the contents of metal elements such as Co, Cu, Ni and REE are depleted, showing unique geochemical characteristics (Kuhn et al., 1998; Josso et al., 2017). Fe-Mn crusts farther away from the hydrothermal field are more likely to be of hydrogenetic origin (such as increased Co and REE content) (Manheim and Lane-Bostwick, 1988; Surya et al., 2020). Therefore, through the investigation and sampling of ferromanganese crusts in the area to be investigated, geochemical research can indicate whether there is hydrothermal activity in the area.

Based on the geochemical analysis of five ferromanganese crust samples collected from the 29–30 ridge segment of the Southwest Indian Ridge, combined with the survey data of the hydrothermal activity in the region, this paper reveals its relationship with the hydrothermal activity in the vicinity.

2 Geological setting

The Southwest Indian Ridge is the boundary between the Antarctic plate and the Indian Ocean plate, with a total length of about 7,700 km, accounting for about 10% of the total length of the mid-ocean ridge (Dick et al., 2003). The full spreading rate of SWIR is about 14–16 mm/yr, belonging to the ultra-slow spreading ridge (Dick et al., 2003). The Andrew Bain transform fault divides SWIR (0–70°E) into two sections, with the western section (0–30°E) having an overall NEE trend and the eastern section (30–70°E) an overall NE trend (DeMets et al., 1990). Our study area is located in the middle of the eastern section of the Southwest Indian Ridge, between the Indomed and Gallieni transform faults. The thickness of the oceanic crust varies greatly. Basalt is mainly exposed on the seabed, and deep

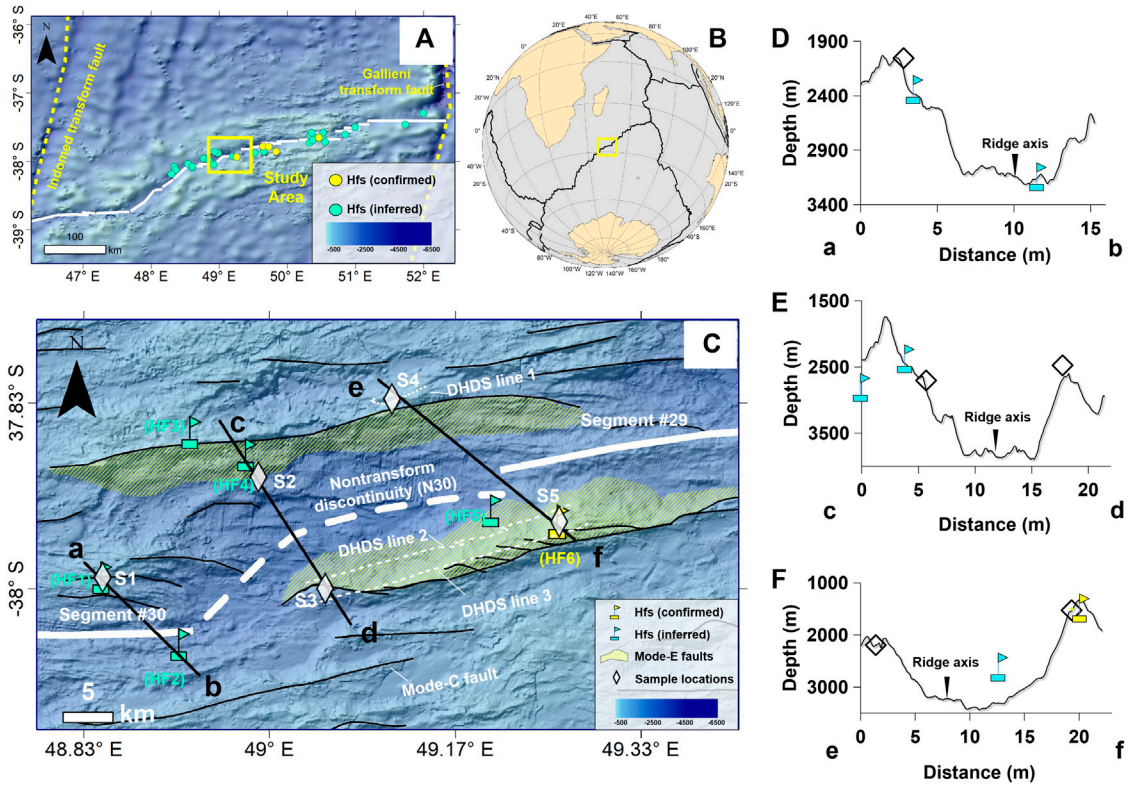

FIGURE 1
Sampling station and geological background. **(A–C)** Topographic map and sampling location of the study area; **(D)** a-b topographic profile; **(E)** c-d topographic profile; **(F)** e-f topographic profile. The white solid line represents the ridge axis, and the white thick dotted line represents the non-transformed discontinuities (NTDs). The white thin dotted line represents the deep-towed survey line. Ridge segmentation and NTDs delimitation are from refs (Cannat et al., 1999; Li et al., 2020). The location information of the seafloor hydrothermal field (HF1-HF6) is from refs (Li et al., 2020; Yue, 2020; Zhang et al., 2022).

TABLE 1 Sampling station information.

Station	Latitude (°S)	Longitude (°E)	Depth (m)	Substrate rock	Crust thickness (mm)
S1	37.99	48.85	2,054	Basalt	5–6
S2	37.90	48.99	2,706	Serpentinite	5–10
S3	38.00	49.05	2,477	Basalt	5–6
S4	37.83	49.11	2,196	Basalt	5–10
S5	37.94	49.26	1,527	Basalt	5–7

oceanic crust and mantle materials are exposed in some areas (Zhou and Dick, 2013). There are 10 central volcanic ridges (AVR) in this region, numbered 25–34 from east to west (Cannat et al., 1999; Li et al., 2020). AVR is offset by nine non-transform discontinuities (NTDs) from 0 to 35 km. The study area is located between 29 and 30 AVR, two AVRs are divided by an NTD, and there is a mode-E type fault on both sides of the ridge axis, with a length of more than 25 km (Liu et al., 2020) (Figure 1). Among them, there are many studies on the mode-E fault located on the south side of the ridge axis. The main part of the fault is oceanic basalt, and the ultramafic rock is exposed at the bottom of the fault, which is in the early stage of detachment fault development.

3 Materials and methods

Five ferromanganese crusts used in this paper were collected by the Chinese "Da Yang Yi Hao" ship in the 29–30 segment of the Southwest Indian Ridge using a television grab during the 2014–2019 marine survey. The sampling location is located on the rift wall 5–7 km away from the ridge axis, and the sampling

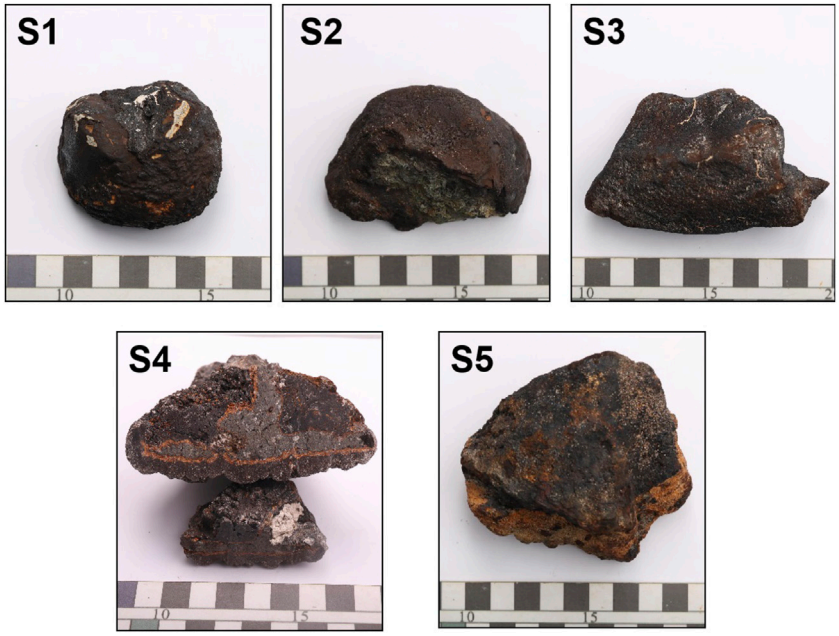

FIGURE 2
Photos of ferromanganese crust samples.

depth ranges from 1,500 to 2,700 m (Figure 1). The sample sampling station information is shown in Table 1.

After cleaning and drying the sample, take a photo of the original sample (Figure 2) and describe the sample. Cut the sample into thin slices using a cutting machine, and perform optical microscopy observation and photography, as shown in Figure 3. The size of the hand specimen to which the ferromanganese crust belongs ranges from 4 to 10 cm, and the thickness of the crust ranges from 5 to 10 mm (Figure 2). The crusts are all black brown in colour, with micro papillary surface morphology. The microscopic observation of ferromanganese crusts in the study area mainly presents parallel layered structures, without obvious sedimentary discontinuities, indicating that the formation environment and material transport of these samples are relatively stable (Figure 3).

After the ferromanganese is peeled off from the original rock, it is cleaned by an ultrasonic cleaning machine with deionized water and ground in an agate mortar to 200 mesh (74 μm). The geochemical analysis of ferromanganese crust samples was carried out in the ALS Laboratory in Guangzhou. The major elements were analyzed by X-ray fluorescence (PANalytical PW2424). Before analysis, each sample is fully mixed with a flux containing Lithium nitrate and heated at 1,000°C for about 1 h. After melting, each sample is transferred to a platinum mould to form a flat glass plate. Three standard samples (GBW07105, NCSDC47009, and SARM-4) were used to monitor the accuracy of data during analysis. The precision of the analysis was better than that of ±5%. Analyze trace elements in Agilent 7700x ICP-MS. Weigh approximately 250 mg of each sample and digest it with $HClO_4$, HNO_3, and HF. Evaporate the solution until dry, discharge the residue, dissolve with dilute HCl, and analyze the dissolved sample. In the spectrum, the results were adjusted based on inter-element interference. The reference samples GBM908-10 and MRGeo08 are used as internal standards for data quality control, the precision of the analysis was better than that of ±10%.

The deep towed hydrothermal detection system (DHDS) was used to investigate the hydrothermal activity of the 29–30 ridge segment of the Southwest Indian Ridge during the 2014–2015 sea survey by the Chinese "Da Yang Yi Hao" ship. The DHDS system includes two cameras that can be used to photograph the seabed and a series of hydrothermal plume detectors (redox potential sensors, turbidity sensors, etc.); among them, the camera was placed on the towed body near the seabed (3–5 m from the bottom), and the hydrothermal plume detectors were placed on the cable of the towed body. Four groups were placed at 50, 100, 150, and 200 m from the bottom, respectively. The deployment test line of DHDS is shown in Figure 1.

4 Results

4.1 Major element

The composition of the bulk chemical major elements of the five ferromanganese crust samples in the study area is shown in Table 2. Among them, the content of Fe and Mn is the highest, and the element content is mostly greater than 10%. Among them, the Fe content ranged from 19.54% to 24.12%, with an average of 22.16%; the Mn content ranges from 6.14% to 15.44%, with an average of 11.58%. The Fe content of crust samples in the study area is significantly higher than that of hydrogenetic ferromanganese crusts in the Northwest Pacific and Indian Ocean, and also

10.3389/feart.2023.1176458

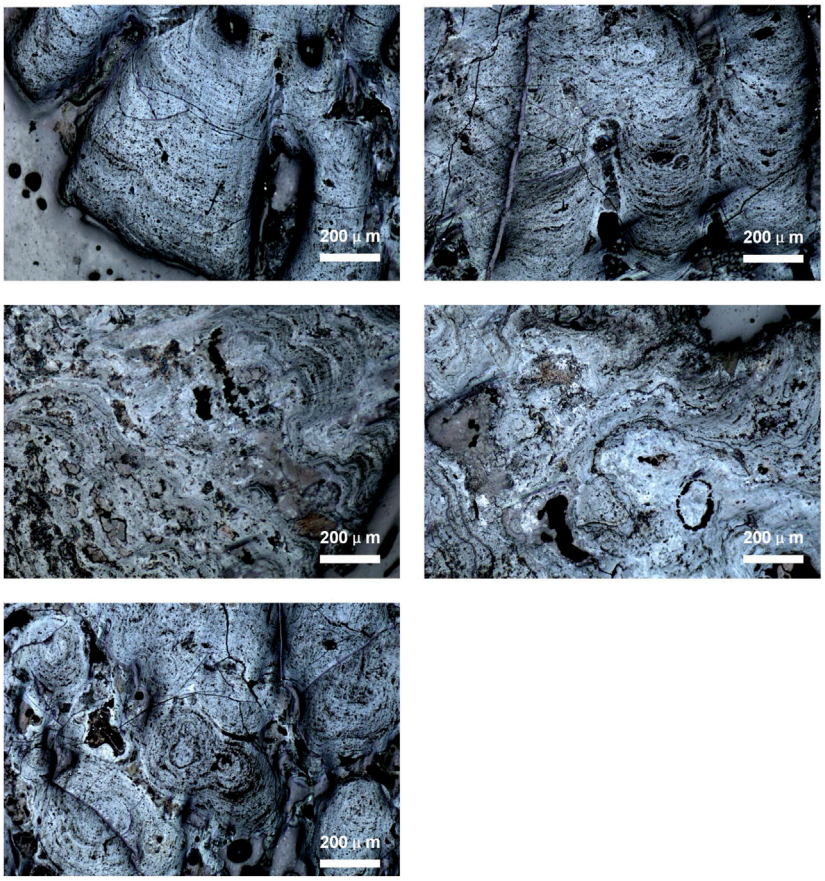

FIGURE 3
Microstructure of ferromanganese crust.

TABLE 2 Major element composition.

Element	Unit	Detection limit	S1	S2	S3	S4	S5	Mean
Fe	wt %	0.01	21.11	19.54	22.42	23.63	24.12	22.16
Mn	wt %	0.01	15.44	12.78	9.96	13.60	6.14	11.58
Si	wt %	0.05	6.55	10.16	8.49	6.16	11.21	8.51
Ca	wt %	0.01	5.98	2.68	4.85	3.49	4.06	4.21
Al	wt %	0.01	3.54	2.70	2.37	1.76	2.29	2.53
Mg	wt %	0.01	3.13	2.17	1.36	1.15	1.82	1.93
Na	wt %	0.01	0.95	1.93	1.79	1.37	1.05	1.42
Ti	wt %	0.01	0.91	0.61	0.61	0.70	0.31	0.63
K	wt %	0.01	0.44	0.49	0.50	0.54	0.72	0.54
P	wt %	0.01	0.46	0.35	0.48	0.52	0.45	0.45
Fe/Mn			1.37	1.54	2.27	1.72	4.00	1.91
Ca/P			13.00	7.66	10.10	6.71	9.02	9.30

higher than that of global ferromanganese nodules (Figure 4). The Mn content is lower than that of hydrogenetic crusts in the Northwest Pacific and Indian Ocean, and also lower than that of global ferromanganese nodules. The Fe/Mn ratio of ferromanganese crusts in the study area is 1.37–4.00, with an average of 1.91, which is significantly higher than that of northwest Pacific crusts (0.68) and

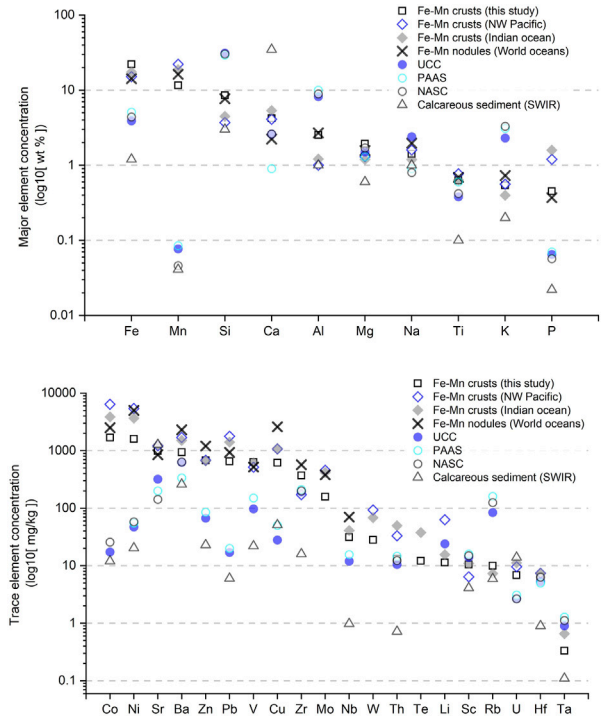

FIGURE 4
Comparison of the bulk chemical major and trace element content of samples in the study area with other samples. The data of Fe-Mn crusts (NW Pacific) are from ref Jamieson and Gartman (2020). The data of Fe-Mn crusts (Indian ocean) are from ref Hein et al. (2016). The Fe-Mn nodules (world ocean) data are from ref Mukhopadhyay et al. (2008). The data of UCC, PAAS and NASC are from ref Ray and Paul (2021). The data of calcareous sediment (SWIR) are from ref Dasong et al. (2016).

Indian Ocean crusts (1.13), and also higher than that of global ferromanganese nodules (0.88) (Figure 4).

The secondary elements are Si, Ca, Al, Mg, and Na, and the element content is mostly between 1% and 10%, with an average content of 8.51%, 4.21%, 2.53%, 1.93%, and 1.42%, respectively (Table 2). Among them, the Si content of the crusts in the study area is significantly higher than that of the hydrogenetic crusts in the Northwest Pacific and Indian Ocean, which is comparable to the global ferromanganese nodules. The Ca content of the crusts in the study area is comparable to that of the Northwest Pacific crusts, slightly lower than that of the Indian Ocean crusts, and significantly higher than that of the global ferromanganese nodules. The Al content of crusts in the study area is significantly higher than that of crusts in the Northwest Pacific and Indian Ocean, which is comparable to that of global ferromanganese nodules. The Mg and Na contents of the crusts in the study area are comparable to those of the Northwest Pacific and Indian Ocean crusts, as well as global ferromanganese nodules. The average contents of Ti, K and P elements in the crust of the study area are lower than 1%, which are 0.63%, 0.54%, and 0.45%, respectively (Table 2).

Among them, the Ti and K contents of the crusts in the study area are equivalent to those of the crusts in the northwest Pacific Ocean and the Indian Ocean, as well as global ferromanganese nodule; The P content of the crusts in the study area is significantly lower than that of the crusts in the Northwest Pacific Ocean and the Indian Ocean and is equivalent to the global ferromanganese nodule. The average Ca/P value of the crusts in the study area is 9.30, which is much higher than that of fluorocarbon Apatite (less than 2), and also significantly higher than that of the crusts in the northwest Pacific Ocean and the Indian Ocean (about 3.4), indicating that there is no obvious phosphorylation of the crusts in the study area (Beaulieu et al., 2015; Surya et al., 2020).

4.2 Trace element

The composition of the bulk chemical trace element of the five ferromanganese crusts in the study area is shown in Table 3. The average content of Co and Ni in ferromanganese crusts in the study area is more than 1,000 mg/kg, and the average content is about 1,600 mg/kg, which is far lower than that in the northwest Pacific, Indian Ocean and global ferromanganese nodule (Figure 4). The average content of Sr, Ba, Zn, Pb, V, Cu, Zr, and Mo in the ferromanganese crusts in the study area ranges from 100 to 1,000 mg/kg. Except for Zn and V, the content of other elements is significantly lower than the hydrogenetic crusts of the Northwest Pacific and Indian Ocean. The Zn content in the crusts of the study area is equivalent to that of the hydrogenetic crusts of the Northwest Pacific Ocean and the Indian Ocean, but significantly lower than that of the global ferromanganese nodule. The V content of crusts in the study area is comparable to that of hydrogenetic crusts in the Northwest Pacific and Indian Ocean, as well as global ferromanganese nodules. The content of Sr in the study area is slightly higher than that of global ferromanganese nodules, and the content of Ba, Pb, Cu, Zr and Mo is significantly lower than that of global ferromanganese nodule. It is worth noting that the Cu element content of S5 is significantly higher, reaching 1.43 wt%, which is 15–31 times the content of the other four samples. Moreover, the Zn content of S5 is significantly higher, approximately twice that of the other four samples. The average content of Nb, W, Th, Te, Li, and Sc in the ferromanganese crusts in the study area ranges from 10 to 50 mg/kg, while the average content of Rb, U, and Hf ranges from 1 to 10 mg/kg. The content of Ta is below 1 mg/kg, with an average of 0.33 mg/kg; Among them, except for the significantly lower content of W, Th, and Te compared to hydrogenetic crusts in the Northwest Pacific and Indian Ocean, the content of other elements is equivalent to that in hydrogenetic crusts in the Northwest Pacific and Indian Ocean.

4.3 Rare earth elements and yttrium

The composition of bulk chemical rare earth elements and yttrium (REY) of the five ferromanganese crusts in the study area is shown in Table 4. The total REE content ranges from 3,208 to 1,415 mg/kg, with an average content of 928 mg/kg, which is lower than that of hydrogenetic ferromanganese crusts (Figure 5). Among them, the total REE content of S5 is very low, which is 320 mg/kg, 2.5–4 times lower than the other four samples. The contents of light rare earth (LREE) and heavy rare earth (HREE) are 285–1,274 mg/kg and 35–140 mg/kg, respectively. LREE/HREE

TABLE 3 Trace element composition.

Element	Unit	Detection limit	S1	S2	S3	S4	S5	Mean
Co	mg/kg	0.1	1,835	1,605	879	1,945	2,210	1,695
Ni	mg/kg	0.2	2,390	2,620	1,015	1,475	515	1,603
Sr	mg/kg	0.2	1,060	923	1,190	1,195	567	987
Ba	mg/kg	0.5	1,040	1,195	990	860	621	941
Zn	mg/kg	2	633	560	449	506	1,250	680
Pb	mg/kg	0.5	754	702	540	1,050	207	651
V	mg/kg	5	672	573	590	744	586	633
Cu	mg/kg	0.2	447	930	599	492	14,300	617[a]
Zr	mg/kg	2	386	395	387	484	201	371
Mo	mg/kg	0.05	238	165.5	76.3	242	69.3	158.0
Nb	mg/kg	0.1	34.0	31.1	32.8	47.6	11.5	31.4
W	mg/kg	1	45	21	14	51	10	28.2
Th	mg/kg	0.01	14.8	10.2	15.1	21.2	4.7	13.2
Te	mg/kg	0.05	13.4	11.5	10.3	18.7	7.2	12.2
Li	mg/kg	0.2	23.2	15.2	5.6	6.2	6.6	11.4
Sc	mg/kg	0.1	10.4	11.8	10.2	10.3	9.8	10.5
Rb	mg/kg	0.1	7.2	8.8	8.0	9.6	16.2	10.0
U	mg/kg	0.05	8.3	5.8	5.7	9.7	4.9	6.9
Hf	mg/kg	0.1	6.0	7.1	7.2	8.7	3.6	6.5
Ta	mg/kg	0.05	0.35	0.33	0.31	0.53	0.14	0.33

[a]Due to the extremely high Cu content of S5 compared to the other four samples, which is not representative, only the average Cu content of S1–S4 is taken for comparison with samples from other regions.

values range from 8.14 to 11.18, with an average of 8.90, which shows light rare earth enrichment. δCe value is 1.50–2.53, with an average of 1.94, indicating that the crust growth environment is partial oxidation. From the normalized distribution curve of rare earth elements of Post-Archean Australian Shales (PAAS) (Figure 5), it can be seen that the five ferromanganese crusts in the study area have a similar distribution trend with hydrogenetic ferromanganese crusts, Ce and Eu elements show obvious positive anomalies and Y elements show obvious negative anomalies except S5. The rare earth curve shows a left-dipping type as a whole, with La_{SN}/Yb_{SN} values ranging from 0.58 to 0.91 and an average of 0.78, showing the enrichment of heavy rare earth relative to shale.

5 Discussion

5.1 Identification of the material source

Fe-(Co + Ni + Cu) × The 10-Mn ternary discriminant diagram is often used to distinguish the material sources of ocean ferromanganese deposits, which are mainly divided into three types of hydrogenetic, hydrothermal and diagenetic genesis (Bau et al., 2014). The ferromanganese crusts of S1-S4 in the study area are in the hydrogenetic origin region of the ternary diagram but are closer to the hydrothermal origin region compared to the hydrogenetic ferromanganese crusts, similar to the ferromanganese crusts affected by the hydrothermal activity (Figure 6A). Among them, the Cu content of S5 is very high, causing a significant deviation from the hydrogenetic region of the ternary diagram. Recently, Josso et al. (2017) used Fe, Mn, Cu, Ni elements, high field strength elements Zr, and rare earth elements Ce, Y to distinguish the material sources of ferromanganese deposits, avoiding the problem of traditional ternary diagrams that are difficult to distinguish between types of hydrogenetic and diagenetic origins. The S1–S4 is in the mixed region of hydrothermal and hydrogenetic genesis, indicating the possible influence of hydrothermal activity (Figure 6B). S5 is close to the diagenetic region due to its high Cu content.

Different types of oceanic ferromanganese deposits have different REY distributions. Bau et al. (2014) distinguished different oceanic ferromanganese deposits using Nd content, Ce and Y anomalies (Figures 7A, B). Among them, hydrothermal deposits have low Nd content, negative Ce anomalies, and positive Y anomalies; Hydrogenetic crusts exhibit high Nd content, positive Ce anomalies, and negative Y anomalies (Bau et al., 2014). In the ferromanganese crusts in the study area,

10.3389/feart.2023.1176458

TABLE 4 Composition of rare earth elements and yttrium.

Element	Unit	Detection limit	S1	S2	S3	S4	S5	Mean	Hydrogenetic Fe-Mn crusts[a]
Y	mg/kg	0.1	140	72	106	158	48	104	175
La	mg/kg	0.1	184	111	170	221	45	146	209
Ce	mg/kg	0.1	572	501	480	775	182	502	700
Pr	mg/kg	0.02	37.8	20.4	35.1	45.3	9.2	29.6	34
Nd	mg/kg	0.1	160	90	152	187	39	125	147
Sm	mg/kg	0.03	31.9	17.5	30.0	36.8	8.1	24.8	28
Eu	mg/kg	0.02	8.3	4.4	7.3	9.5	2.3	6.4	7.5
Gd	mg/kg	0.05	35.8	19.9	32.6	41.5	9.5	27.9	35
Tb	mg/kg	0.01	5.5	3.1	5.0	6.3	1.5	4.2	5.6
Dy	mg/kg	0.05	32.9	18.3	29.9	38.4	9.4	25.8	35.9
Ho	mg/kg	0.01	6.8	3.7	5.7	7.8	2.0	5.2	8.1
Er	mg/kg	0.03	19.0	10.3	15.8	21.8	5.8	14.5	25.1
Tm	mg/kg	0.01	2.6	1.4	2.1	3.0	0.8	2.0	3.6
Yb	mg/kg	0.03	16.2	8.6	12.6	18.7	5.3	12.3	24.4
Lu	mg/kg	0.01	2.6	1.3	1.9	2.9	0.9	1.9	3.8
∑REE	mg/kg		1,115	811	979	1,415	320	928	1,267
LREE	mg/kg		993	744	874	1,274	285	834	1,125
HREE	mg/kg		121	67	106	140	35	94	142
LREE/HREE			8.19	11.18	8.28	9.08	8.14	8.90	7.90
δCe			1.65	2.53	1.50	1.86	2.14	1.94	2.07
La_{SN}/Yb_{SN}			0.77	0.86	0.91	0.80	0.58	0.78	0.58

Note: δ Ce = $2Ce_{SN}/(La_{SN} + Pr_{SN})$, Ce_{SN}, La_{SN}, and Pr_{SN} are the normalized values of Post-Archean Australian Shales. Shale data from ref Pourmand et al. (2012).
[a]The data is the average from the literature (Bau et al., 1996).

S3 exhibits weak Ce negative anomalies, while S1, S4, and S5 exhibit weak Ce positive anomalies, between typical hydrogenetic crusts and hydrothermal ferromanganese oxides, indicating that they may be affected by hydrothermal activity (Figure 7A). The Ce positive anomaly of S2 is slightly higher than that of the other four samples, but it is also significantly lower than typical hydrogenetic crusts, and the Nd content is also significantly lower than that of hydrogenetic crusts, indicating that it may be affected by hydrothermal activity (Figure 7A). All five crusts in the study area exhibit weak Y negative anomalies, Ce weak positive or weak negative anomalies, and are in the transition zone between hydrogenetic crusts and hydrothermal ferromanganese oxides, indicating the possible influence of hydrothermal activity (Figure 7B). The Co and REE elements in ferromanganese crusts mainly come from seawater, which is often enriched in hydrogenetic crusts and depleted in hydrothermal crusts (reference). In addition, there are significant differences in Mn/Fe values among ferromanganese deposits of different origins. Hydrothermal ferromanganese deposits often exhibit significant differentiation between Fe and Mn, with high Fe and low Mn being common, indicating low Mn/Fe values (Manheim and Lane-Bostwick, 1988). The Co and REE content of crusts in the study area is between the hydrogenetic crusts and the hydrothermal ferromanganese deposits, with the characteristics of hydrogenetic and hydrothermal mixing (Figures 7C, D). The Mn/Fe value of the crust in the study area is slightly lower than that of typical hydrogenetic crusts, indicating possible hydrothermal activity effects (Figure 7C).

5.2 Indication of off-axis hydrothermal activity

Previous investigations have shown that there is one confirmed Yuhuang-1 hydrothermal field (Figure 1, HF6) and five inferred hydrothermal fields (Figure 1, HF1-HF5) in the study area (Li et al., 2020; Yue, 2020; Zhang et al., 2022). Among them, three are inferred active hydrothermal fields (HF2: S30 hydrothermal field, HF3: Yuhuang-3 hydrothermal field, HF5: Yuhuang-2 hydrothermal field), and there are also water turbidity anomalies and ORP anomalies (Li et al., 2020). There are also two inferred inactive hydrothermal fields (HF1: Baidi hydrothermal field and HF4: Chunxi hydrothermal field). Alteration rocks and hydrothermal products (opals) related to hydrothermal activity were found, but no turbidity anomaly of the water column was found (Tao et al., 2012). Except that the HF2 hydrothermal anomaly field is located near the ocean ridge axis (<3 km), the other hydrothermal fields or

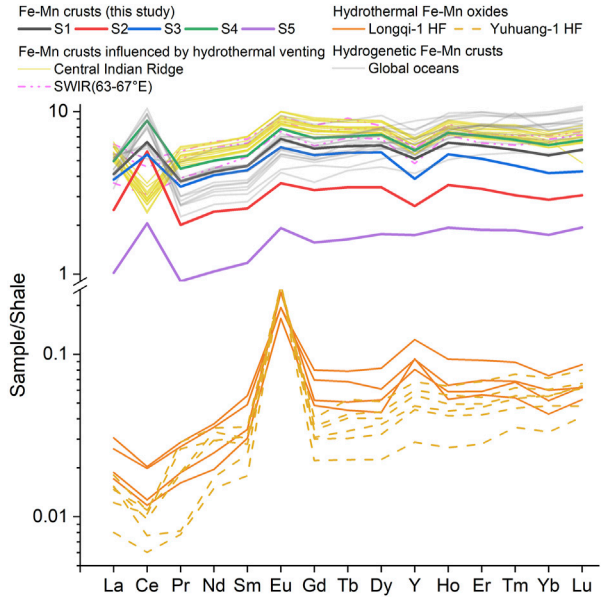

FIGURE 5
Range of shale-normalized rare-earth element (REE) and Y. Shales data of Post-Archean Australian comes from ref Pourmand et al. (2012). The data of hydrothermal Fe-Mn oxides are from refs Ye (2010) and Hu et al. (2022). The data of hydrogenetic ferromanganese crusts are from ref Bau et al. (2014). Data on Fe-Mn crusts influenced by hydrothermal venting come from refs Kuhn et al. (1998) and Surya et al. (2020).

hydrothermal anomaly fields are located in the off-axis area (5–10 km) on both sides of the ocean ridge axis.

The previous investigation showed that the diffusion range of the hydrothermal plume in the Southwest Indian Ridge was not more than 10 km, and most of them were less than 5 km (Yue et al., 2019; Chen et al., 2021). After being more than 10 km away from the hydrothermal activity field, many parameters for tracing the hydrothermal plume decrease to lower levels, close to the background seawater (Yue et al., 2019; Chen et al., 2021). In addition, the geochemical analysis of the surface sediments around the hydrothermal field also shows that the chemical anomaly of the sediments affected by the hydrothermal substances has significantly decreased to the level close to the background sediments after being more than 10 km away from the hydrothermal activity field (Liao et al., 2018; Liao et al., 2019).

Among the ferromanganese crusts sampled in the study area, S1 was taken from the vicinity of the Baidi hydrothermal field (~2 km), S2 was taken from the vicinity of the Chunxi hydrothermal field (~2 km), S5 was taken from the confirmed Yuhuang-1 hydrothermal field. To sum up, the content of Cu and Zn in S5 is significantly higher, especially the very high content of Cu, which may be related to the abundant supply of Cu and Zn in the hydrothermal field. In addition, the REE content of S5 is significantly lower than that of aqueous crusts and the other four crusts, which is also similar to that of hydrothermal products. In addition to S5 affected by hydrothermal activity, the other four crust samples may also be affected by hydrothermal activity to a certain

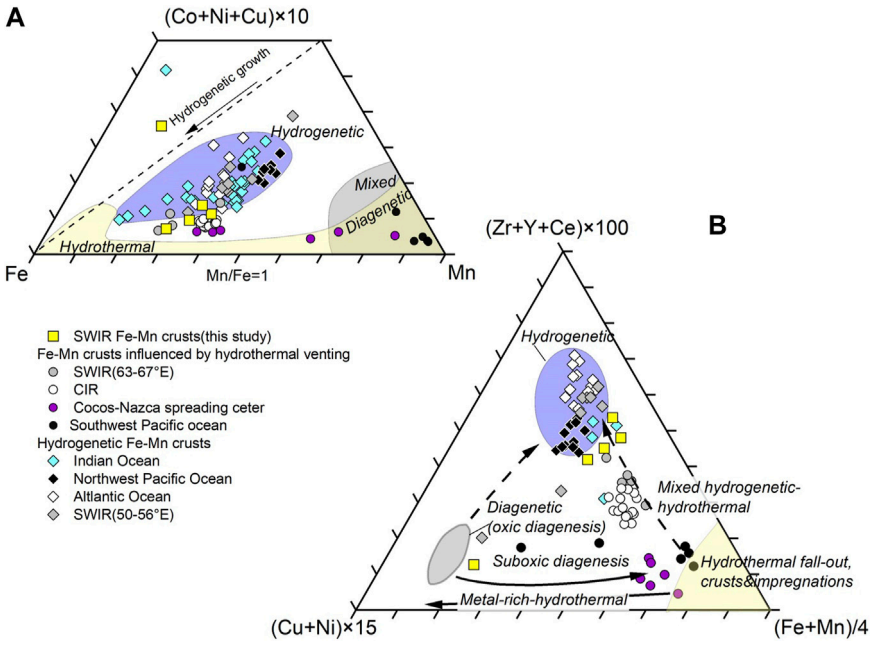

FIGURE 6
Ternary discriminant diagram of ferromanganese crust. **(A)** Fe-(Co + Ni + Cu) × 10-Mn ternary discriminant diagram, modified from ref Bonatti et al. (1972); **(B)** 15 × (Cu + Ni)-(Zr + Y + Ce) × 100-(Fe + Mn)/4, modified from ref Josso et al. (2017). Data on hydrogenetic ferromanganese crusts from refs Yu et al. (2013), Bau et al. (2014), and Yu et al. (2021); Data of Fe-Mn crusts influenced by hydrothermal venting are from refs Kuhn et al. (1998), Surya et al. (2020), Staszak et al. (2022), and Zawadzki et al. (2022).

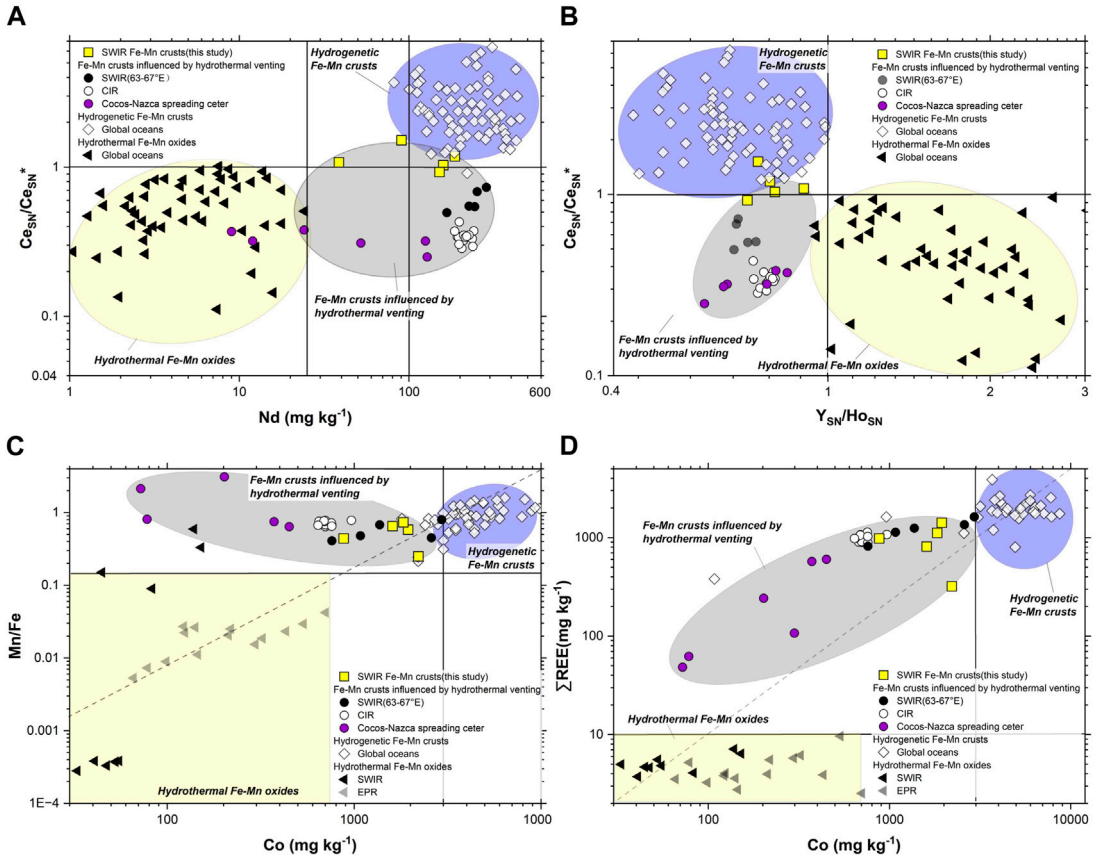

FIGURE 7
Bivariate discriminant diagram of ferromanganese crust. **(A)** Ce_{SN}/Ce_{SN}* ratio vs. Nd content; **(B)** Ce_{SN}/Ce_{SN}* ratio vs Y_{SN}/Ho_{SN} ratio; **(C)** Mn/Fe ratio vs Co content; **(D)** Total REE content vs Co content. The data of hydrogenetic ferromanganese crusts are from Bau et al. (2014); The data of Fe-Mn crusts influenced by hydrothermal venting are from refs (Kuhn et al., 1998; Surya et al., 2020; Zawadzki et al., 2022); The data of hydrothermal Fe-Mn oxides are from refs (Zhigang et al., 2007; Ye, 2010; Bau et al., 2014; Hu et al., 2022).

FIGURE 8
Photographs of altered rocks near the S3 station.

extent, thus showing characteristics different from common hydrogenetic crusts (Figures 6, 7). S3 and S4 are more than 10 km away from the known hydrothermal field or hydrothermal anomaly field, which exceeds the diffusion range of the hydrothermal plume in this region. The influence of hydrothermal activity on these two ferromanganese crusts may come from the undiscovered hydrothermal field.

On DHDS survey line 2, adjacent to the S3 station area, a large area of yellowish-brown breccia covered by thin sediment layers was observed in seabed photography (Figure 8), suspected to have been

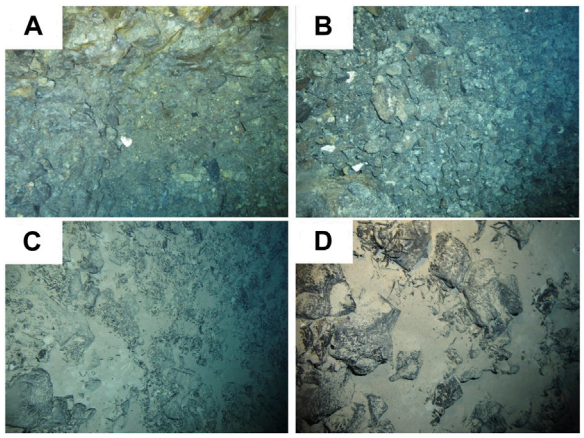

FIGURE 9
Photographs of seabed near S4 station. **(A,B)** Altered rocks; **(C,D)** Suspected hydrothermal biological remains.

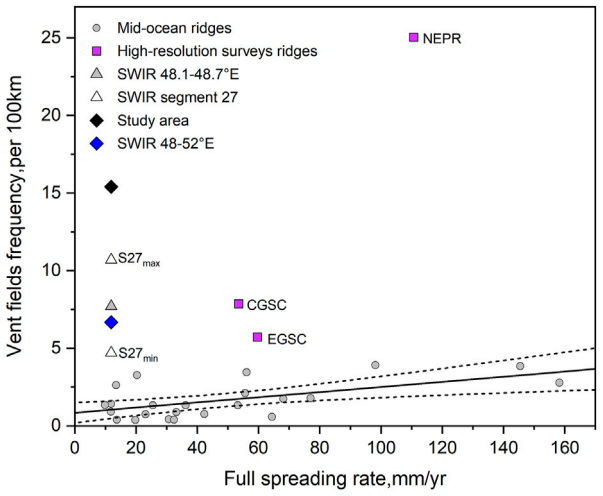

FIGURE 10
The relationship between the spatial frequency of hydrothermal activity and the spreading rate of the oceanic spreading ridge. The grey circle data is from ref Beaulieu et al. (2015), representing the well-surveyed area; The purple square data comes from ref Baker et al. (2016), representing the area of detailed optical and ORP survey. CGSC is the Galapagos spreading centre, EGSC is the east side of Galapagos spreading centre, and NEPR is 9–10°N of the East Pacific Rise; The black diamond is the data of the study area; The grey triangle data is from ref Chen et al. (2021), which represents the area between SWIR 30 and 31 ridge segments of the detailed optical and ORP survey; The white triangle data is from ref Yue et al. (2019), representing the SWIR 27 ridge segment of the detailed optical and ORP survey; The blue diamond is a synthesis of the research results of this paper and the publicly reported data of the hydrothermal fields in the SWIR 48–52°E area. The black line represents the linear regression fitting line of the well-surveyed ridges, and the black dotted line represents the ±95% confidence interval.

modified by surrounding hydrothermal fluids. The hydrothermal plume sensor deployed on the survey line did not record any water column anomalies. On DHDS Line 3, adjacent to S3 station, the hydrothermal plume sensor deployed recorded a significant sudden increase in water turbidity and a sudden decrease in oxidation Reduction potential near 2,200 m water depth (Li et al., 2015); In summary, there is a high possibility of an unknown hydrothermal field near the S3 station, and we have temporarily named it the 49.05°E hydrothermal field.

On the DHDS survey line 1, a large area of yellowish-brown rock was observed in the seabed camera near the S4 station (Figure 9), which is different from the mid-ocean ridge basement rock dominated by grey-black oceanic basalt and is suspected to be modified by the surrounding high-temperature hydrothermal fluid (Tao et al., 2012; Chen et al., 2021). The hydrothermal plume sensor did not record the water chemistry and water turbidity anomalies, indicating that the hydrothermal activity in this area may be inactive. In addition, the seabed camera also observed a large area of dead shell remnants (Figure 9), suspected to be mussels living near the hydrothermal field (Tao et al., 2012). This also further proves that there is seafloor hydrothermal activity in this area, which has ceased. In summary, there is a high possibility that there is an unknown hydrothermal field near the S4 station. We temporarily named it the 49.11°E hydrothermal field.

Together with the two off-axis hydrothermal fields identified in this paper, a total of eight hydrothermal fields were found in the 29–30 ridge segment of the Southwest Indian Ridge, of which only one was near the ridge axis and the remaining seven were located in the off-axis 5–10 km region (Figure 1), showing high off-axis hydrothermal activity abundance. In the region with a total length of about 52 km, the spatial frequency of hydrothermal activity (Fs) is 15.4 sites/100 km. It is significantly higher than the well-investigated ocean ridge and 14 times higher than the linear fit prediction (Fs: 1.1 sites/100 km) (Figure 10). Compared to other detailed hydrothermal activity surveys on the Southwest Indian Ridge, the Fs of the study area is at a high level. Among them, the Fs of the study area is twice as high as that of the adjacent SWIR 48.1–48.7°E region located on its western side, which is 44% higher than the highest prediction of the SWIR 27 segment on the east side of the study area. The study area also had a higher Fs than other well-investigated spreading centres, one time higher than the Galapagos spreading centre, but significantly lower than the North East Pacific Rise. This means that the off-axis hydrothermal activity of the Southwest Indian Ridge is still underestimated compared to past understanding.

5.3 Factors controlling the distribution of hydrothermal activity

The seafloor hydrothermal circulation is ultimately driven by heat sources, and magmatic activity can provide sufficient heat sources for hydrothermal activity. The variability of magma supply is the main controlling factor affecting the distribution pattern of hydrothermal activity on the mid-ocean ridge, and hydrothermal activity increases linearly with the increase of magma supply (Beaulieu et al., 2015; Baker, 2017). Due to the influence of segmentation and local magma supply characteristics, there are differences in the amount of magma and the proportion of tectonic activity between different ridge segments in the Southwest Indian Ocean. This in turn leads to the diversity of

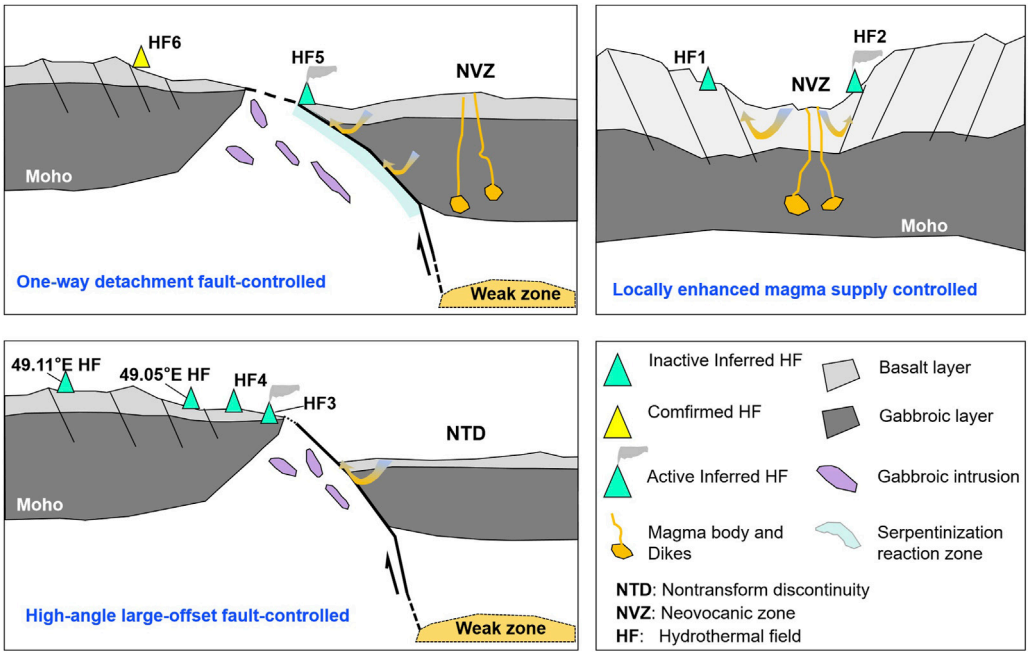

FIGURE 11
Hydrothermal circulation system model in the study area [Modified from Tao et al. (2023)].

heat sources and channels in the hydrothermal circulation system, ultimately resulting in a rich diversity of hydrothermal activities (Tao et al., 2020; Wu et al., 2021; Zhou et al., 2022; Tao et al., 2023). Tao et al. (2023) divided the hydrothermal circulation of the Southwest Indian Ridge into four types: localized strong magmatic supply-controlled type, high angle large offset fault controlled type, one-way detachment fault controlled type, and flip-flop detachment fault controlled type. In this study area, the Baidi hydrothermal field (HF1) is classified as a localized strong magmatic supply-controlled type, the Yuhuang-1 hydrothermal field (HF6) is classified as a one-way detachment fault-controlled type, and the Chunxi hydrothermal field (HF4) is classified as high angle large offset fault controlled type (Tao et al., 2023).

According to the above classification method of Hydrothermal circulation, other hydrothermal fields in this study area are classified as follows, and the model of the hydrothermal circulation system in this study area is summarized in Figure 11. Yuhuang-2 hydrothermal field (HF5) and Yuhuang-1 hydrothermal field are located on the Yuhuang detachment fault (Chen et al., 2023), both controlled by detachment faults and should be classified as one-way detachment fault controlled Hydrothermal circulation. Yuhuang-3 hydrothermal field (HF3), 49.05° E hydrothermal field and 49.11° E hydrothermal field are all located on Mode-E fault (also can be expressed as high angle and large offset normal fault), similar to Chunxi hydrothermal field, and should be classified as high angle large offset fault controlled Hydrothermal circulation; Among them, the Yuhuang-3 hydrothermal field, Chunxi hydrothermal field, and 49.11°E hydrothermal field are all located on the same Mode-E fault on the north side of Nontransform discontinuity (N30), while the 49.05° E hydrothermal field is located on the Mode-E fault on the south side of N30. The heat source of one-way detachment fault-controlled Hydrothermal circulation is similar to that of high angle large offset fault-controlled Hydrothermal circulation. It is a local high-temperature Gabbro intrusion or deep high-temperature mantle, and the hydrothermal circulation channels are respectively deep detachment faults and high angle and large offset faults (Tao et al., 2023).

The S30 hydrothermal field (HF2) is similar to the Baidi hydrothermal field, both located near the neovolcanic ridge of the #30 segment, and should be classified as a localized strong magmatic supply-controlled type; Among them, the Baidi hydrothermal field is located on the north side of #30 segment, and the S30 hydrothermal field is located on the south side of this ridge segment. In this kind of localized strong magmatic supply-controlled Hydrothermal circulation, the magma intruded from the axis becomes the heat source of the hydrothermal circulation system, and the axial fault provides a channel for fluid migration (Tao et al., 2023).

6 Conclusion

In this paper, the abundant off-axis hydrothermal activity of the 29–30 ridge of the Southwest Indian Ocean Ridge was studied. By analyzing the chemical composition and REE composition of ferromanganese crusts, the influence of hydrothermal activities on the origin and evolution of ferromanganese crusts and the controlling factors of the distribution of hydrothermal activities were discussed. The main conclusions are as follows:

1. The crust samples in the study area have low Co and rare earth element contents, and the material source discrimination diagram reveals that they have a mixed hydrogenetic and hydrothermal origin;
2. Identify two unknown seafloor hydrothermal fields, one of which is an inactive hydrothermal field, and obtain evidence from

seabed camera images. Based on the geochemical survey of ferromanganese crusts, it can be an effective means of investigating inactive seafloor hydrothermal activity;

3. The spatial frequency of hydrothermal activity in the study area reaches 15 sites/100 km, which is significantly higher than other well-investigated oceanic ridges, indicating that the Southwest Indian Ridge still has high potential for hydrothermal activity investigation;
4. The control factors of hydrothermal activity in the study area are diverse, including localized strong magmatic supply-controlled type, high angle large offset fault controlled type, one-way detachment fault controlled type.

Data availability statement

The original contributions presented in the study are included in the article/supplementary material, further inquiries can be directed to the corresponding author.

Author contributions

CT led the project and finished the interpretation. XY prepared the original manuscript, analyses and geochemistry interpretation. SL participated in the interpretation of the results. All authors contributed to the article and approved the submitted version.

Funding

This research was funded by the National Natural Science Foundation of China (42127807 and 42006074), the Key R&D Program of Zhejiang Province (2021C03016), and the China Ocean Mineral Resources R&D Association Project (DY135-S1-1-02, 08).

Acknowledgments

We would like to thank the captains and crews who contributed to the success of this project.

Conflict of interest

The authors declare that the research was conducted in the absence of any commercial or financial relationships that could be construed as a potential conflict of interest.

Publisher's note

References

Baker, E. (2017). Exploring the ocean for hydrothermal venting: new techniques, new discoveries, new insights. *Ore Geol. Rev.* 86, 55–69. doi:10.1016/j.oregeorev.2017.02.006

Baker, E. T., Resing, J. A., Haymon, R. M., Tunnicliffe, V., Lavelle, J. W., Martinez, F., et al. (2016). How many vent fields? New estimates of vent field populations on ocean ridges from precise mapping of hydrothermal discharge locations. *Earth Planet. Sci. Lett.* 449, 186–196. doi:10.1016/j.epsl.2016.05.031

Bau, M., Koschinsky, A., Dulski, P., and Hein, J. R. (1996). Comparison of the partitioning behaviours of yttrium, rare earth elements, and titanium between hydrogenetic marine ferromanganese crusts and seawater. *Geochimica Cosmochimica Acta* 60 (10), 1709–1725. doi:10.1016/0016-7037(96)00063-4

Bau, M., Schmidt, K., Koschinsky, A., Hein, J., Kuhn, T., and Usui, A. (2014). Discriminating between different genetic types of marine ferro-manganese crusts and nodules based on rare earth elements and yttrium. *Chem. Geol.* 381, 1–9. doi:10.1016/j.chemgeo.2014.05.004

Beaulieu, S. E., Baker, E. T., and German, C. R. (2015). Where are the undiscovered hydrothermal vents on oceanic spreading ridges? *Deep Sea Res. Part II* 121, 202–212. doi:10.1016/j.dsr2.2015.05.001

Beaulieu, S. E., and Szafrański, K. M. (2020). *InterRidge global database of active submarine hydrothermal vent fields*. United States: PANGAEA. doi:10.1594/PANGAEA.917894

Bonatti, E., Kraemer, T., and Rydell, H. (1972). Classification and genesis of submarine iron-manganese deposits. in *Ferromanganese deposits on the ocean floor* (Berlin, Germany: Springer), 149–166.

Cannat, M., Rommevaux-Jestin, C., Sauter, D., Deplus, C., and Mendel, V. (1999). Formation of the axial relief at the very slow spreading Southwest Indian Ridge (49° to 69°E). *J. Geophys. Res.* 104 (10), 22825–22843. doi:10.1029/1999JB900195

Chen, D., Tao, C., Wang, Y., Chen, S., Liang, J., Liao, S., et al. (2021). Seafloor hydrothermal activity around a large non-transform discontinuity along ultraslow-spreading southwest Indian ridge (48.1–48.7° E). *J. Mar. Sci. Eng.* 9 (8), 825. doi:10.3390/jmse9080825

Chen, J., Zhang, T., Li, H., Tao, C., Cannat, M., and Sauter, D. (2023). Evolution of enhanced magmatism at the ultraslow spreading Southwest Indian Ridge between 46°E and 53.5°E. *Tectonophysics* 860, 229903. doi:10.1016/j.tecto.2023.229903

Dasong, H., Xiaoyu, Z., Guoyin, Z., Chunhui, T., and Huaiming, L. (2016). Geochemical characteristics of sediments in southwest Indian ridge48.6°-51.7°E. *Geol. Sci. Technol. Inf.* 35 (1), 8.

DeMets, C., Gordon, R. G., Argus, D. F., and Stein, S. (1990). Current plate motions. *Geophys. J. Int.* 101 (2), 425–478. doi:10.1111/j.1365-246X.1990.tb06579.x

Dick, H. J. B., Lin, J., and Schouten, H. (2003). An ultraslow-spreading class of ocean ridge. *Nature* 426 (6965), 405–412. doi:10.1038/nature02128

Escartín, J., Smith, D. K., Cann, J., Schouten, H., Langmuir, C. H., and Escrig, S. (2008). Central role of detachment faults in accretion of slow-spreading oceanic lithosphere. *Nature* 455 (7214), 790–794. doi:10.1038/nature07333

Fouquet, Y., Cambon, P., Etoubleau, J., Charlou, J. L., OndréAs, H., Barriga, F. J. A. S., et al. (2010). "Geodiversity of hydrothermal processes along the Mid-Atlantic Ridge and ultramafic-hosted mineralization: a new type of oceanic Cu-Zn-Co-Au volcanogenic massive sulfide deposit," in *Diversity of hydrothermal systems on slow spreading ocean ridges* (Berlin, Germany: Springer), 321–367.

German, C. R., Petersen, S., and Hannington, M. D. (2016). Hydrothermal exploration of mid-ocean ridges: where might the largest sulfide deposits be forming? *Chem. Geol.* 420, 114–126. doi:10.1016/j.chemgeo.2015.11.006

Hannington, M. D., De Ronde, C. E. J., Petersen, S., Hedenquist, J. W., Thompson, J. F. H., Goldfarb, R. J., et al. (2005). "Sea-floor tectonics and submarine hydrothermal systems," in *One hundredth anniversary volume* (United States: Society of Economic Geologists).

Hannington, M., Jamieson, J., Monecke, T., Petersen, S., and Beaulieu, S. (2011). The abundance of seafloor massive sulfide deposits. *Geology* 39 (12), 1155–1158. doi:10.1130/G32468.1

Hein, J. R., Conrad, T., Mizell, K., Banakar, V. K., Frey, F. A., and Sager, W. W. (2016). Controls on ferromanganese crust composition and reconnaissance resource potential, Ninetyeast Ridge, Indian Ocean. *Deep Sea Res. Part I* 110, 1–19. doi:10.1016/j.dsr.2015.11.006

Hein, J. R., and Koschinsky, A. (2014). "Deep-Ocean ferromanganese crusts and nodules," in *Treatise on geochemistry* Editors H. D. Holland and K. K. Turekian Second Edition (Oxford: Elsevier), 273–291.

Hu, S., Tao, C., Liao, S., Zhu, C., and Qiu, Z. (2022). Transformation of minerals and mobility of heavy metals during oxidative weathering of seafloor massive sulfide and their environmental significance. *Sci. Total Environ.* 819, 153091. doi:10.1016/j.scitotenv.2022.153091

Jamieson, J., and Gartman, A. (2020). Defining active, inactive, and extinct seafloor massive sulfide deposits. *Mar. Policy* 117, 103926. doi:10.1016/j.marpol.2020.103926

Josso, P., Pelleter, E., Pourret, O., Fouquet, Y., Etoubleau, J., Cheron, S., et al. (2017). A new discrimination scheme for oceanic ferromanganese deposits using high field strength and rare earth elements. *Ore Geol. Rev.* 87, 3–15. doi:10.1016/j.oregeorev.2016.09.003

Kuhn, T., Bau, M., Blum, N., and Halbach, P. (1998). Origin of negative Ce anomalies in mixed hydrothermal–hydrogenetic Fe–Mn crusts from the Central Indian Ridge. *Earth Planet. Sci. Lett.* 163 (1), 207–220. doi:10.1016/S0012-821X(98)00188-5

Li, H., Lei, J., Zhang, K., and Sun, Y. (2015). *China Ocean Mineral Resources R&D association 34th cruise leg 2 cruise report*. Beijing: China Ocean Mineral Resources R&D Association.

Li, H., Tao, C., Yue, X., Baker, E. T., Deng, X., Zhou, J., et al. (2020). Enhanced hydrothermal activity on an ultraslow-spreading supersegment with a seismically detected melting anomaly. *Mar. Geol.* 430, 106335. doi:10.1016/j.margeo.2020.106335

Liao, S., Tao, C., Dias, A. A., Su, X., Yang, Z., Ni, J., et al. (2019). Surface sediment composition and distribution of hydrothermal derived elements at the Duanqiao-1 hydrothermal field, Southwest Indian Ridge. *Mar. Geol.* 416, 105975. doi:10.1016/j.margeo.2019.105975

Liao, S., Tao, C., Li, H., Zhang, G., Liang, J., Yang, W., et al. (2018). Surface sediment geochemistry and hydrothermal activity indicators in the Dragon Horn area on the Southwest Indian Ridge. *Mar. Geol.* 398, 22–34. doi:10.1016/j.margeo.2017.12.005

Liu, C., Li, J., Tao, C., Fan, Q., Song, J., Luo, Y., et al. (2020). Variations in faulting style of the Southwest Indian ridge (46°–53.5°E): implications for crustal accretion process at ultraslow-spreading ridges. *Tectonophysics* 790, 228552. doi:10.1016/j.tecto.2020.228552

Manheim, F. T., and Lane-Bostwick, C. M. (1988). Cobalt in ferromanganese crusts as a monitor of hydrothermal discharge on the Pacific sea floor. *Nature* 335 (6185), 59–62. doi:10.1038/335059a0

Mukhopadhyay, R., Ghosh, A. K., and Iyer, S. D. (2008). "Ferromanganese deposits," in *Handbook of exploration and environmental geochemistry* (Netherlands: Elsevier Science BV), 155–224.

Pourmand, A., Dauphas, N., and Ireland, T. J. (2012). A novel extraction chromatography and MC-ICP-MS technique for rapid analysis of REE, Sc and Y: revising CI-chondrite and post-archean Australian shale (PAAS) abundances. *Chem. Geol.* 291, 38–54. doi:10.1016/j.chemgeo.2011.08.011

Ray, E., and Paul, D. (2021). Major and trace element characteristics of the average Indian post-archean shale: implications for provenance, weathering, and depositional environment. *ACS Earth Space Chem.* 5 (5), 1114–1129. doi:10.1021/acsearthspacechem.1c00030

Staszak, P., Collot, J., Josso, P., Pelleter, E., Etienne, S., Patriat, M., et al. (2022). Origin and composition of ferromanganese deposits of New Caledonia exclusive economic zone. *Minerals* 12, 255. doi:10.3390/min12020255

Surya, P., Ray, D., Kurian, J. P., M., S., K.a., K. R., et al. (2020). Anomalous phase association of REE in ferromanganese crusts from Indian mid-oceanic ridges: evidence for large scale dispersion of hydrothermal iron. *Chem. Geol.* 549, 119679. doi:10.1016/j.chemgeo.2020.119679

Tao, C., Guo, Z., Liang, J., Ding, T., Yang, W., Liao, S., et al. (2023). Sulfide metallogenic model for the ultraslow-spreading Southwest Indian Ridge. *Sci. China Earth Sci.* 66 (6), 1212–1230. doi:10.1007/s11430-023-1108-7

Tao, C., Lin, J., Guo, S., Chen, Y. J., Wu, G., Han, X., et al. (2012). First active hydrothermal vents on an ultraslow-spreading center: southwest Indian ridge. *Geology* 40 (1), 47–50. doi:10.1130/g32389.1

Tao, C., Seyfried, W. E., Jr., Lowell, R. P., Liu, Y., Liang, J., Guo, Z., et al. (2020). Deep high-temperature hydrothermal circulation in a detachment faulting system on the ultra-slow spreading ridge. *Nat. Commun.* 11 (1), 1300. doi:10.1038/s41467-020-15062-w

Tivey, M. A., Schouten, H., and Kleinrock, M. C. (2003). A near-bottom magnetic survey of the Mid-Atlantic Ridgeridge axis at 26°N: implications for the tectonic evolution of the TAG segment. *J. Geophys. Res.* 108 (5). doi:10.1029/2002JB001967

Wu, T., Tivey, M. A., Tao, C., Zhang, J., Zhou, F., and Liu, Y. (2021). An intermittent detachment faulting system with a large sulfide deposit revealed by multi-scale magnetic surveys. *Nat. Commun.* 12 (1), 5642. doi:10.1038/s41467-021-25880-1

Ye, J. (2010). *Mineralization of polymetallic sulfides on ultra-slow spreading southwest indian ridge at 49.6°E(Chineses)*. doctor of philosophy doctor (China: Graduate university of Chinese academy of sciences).

Yu, J., Tao, C., Liao, S., Dias, A. A., Liang, J., Yang, W., et al. (2021). Resource estimation of the sulfide-rich deposits of the Yuhuang-1 hydrothermal field on the ultraslow-spreading Southwest Indian Ridge. *Ore Geol. Rev.* 134, 104169. doi:10.1016/j.oregeorev.2021.104169

Yu, Z., Fan, D., Zhang, A., Sun, X., and Yang, Z. (2013). Mineralogy and geochemistry of cobalt-rich crusts from the Southwest Indian Ridge. *Mar. Geol. Quat. Geol.* 33 (6), 10.

Yue, X., Li, H., Ren, J., Tao, C., Zhou, J., Wang, Y., et al. (2019). Seafloor hydrothermal activity along mid-ocean ridge with strong melt supply: study from segment 27, southwest Indian ridge. *Sci. Rep.* 9 (1), 9874. doi:10.1038/s41598-019-46299-1

Yue, X. (2020). *Seafloor hydrothermal activity along the mid-ocean ridge with high melt supply: study from segment 27, Southwest Indian Ridge(Chineses)*. doctor (China: China University of Geosciences).

Zawadzki, D., Maciąg, Ł., Blasco, I., González, F. J., Wernette, B., Marino, E., et al. (2022). Geochemistry and mineralogy of ferromanganese crusts from the western cocos-nazca spreading centre, pacific. *Minerals* 12 (5), 538. doi:10.3390/min12050538

Zhang, L., Tao, C., Su, X., Lv, S., Zhou, J., Deng, X., et al. (2022). Characteristics of rare earth elements in the surface sediments of southwest Indian ridge: implication of grain size for the identification of hydrothermal activity. *Geo-Marine Lett.* 42 (1), 7. doi:10.1007/s00367-022-00729-8

Zhigang, Z., Xiaoyuan, W., Guoliang, Z., Xuebo, Y., Daigeng, C., and Xiaomei, W. (2007). Formation of Fe-oxyhydroxylation near 13 ° N of the East pacific Rise: mineral and geochemical evidence. *Chin. Sci. earth Sci.* 37 (10), 1349–1357.

Zhou, F., Dyment, J., Tao, C., and Wu, T. (2022). Magmatism at oceanic core complexes on the ultraslow southwest Indian ridge: insights from near-seafloor magnetics. *Geology* 50 (6), 726–730. doi:10.1130/G49771.1

Zhou, H., and Dick, H. J. B. (2013). Thin crust as evidence for depleted mantle supporting the Marion Rise. *Nature* 494 (7436), 195–200. doi:10.1038/nature11842